nature nanotechnology

Article

https://doi.org/10.1038/s41565-023-01543-8

Efficient multicarbon formation in acidic CO_2 reduction via tandem electrocatalysis

Received: 26 October 2022

Accepted: 12 October 2023

Published online: 23 November 2023

Check for updates

Yuanjun Chen[1,8], Xiao-Yan Li[1,8], Zhu Chen[1,8], Adnan Ozden[2], Jianan Erick Huang[1], Pengfei Ou[1], Juncai Dong[3], Jinqiang Zhang[1], Cong Tian[1], Byoung-Hoon Lee[1,4], Xinyue Wang[1], Shijie Liu[2], Qingyun Qu[5], Sasa Wang[1], Yi Xu[2], Rui Kai Miao[2], Yong Zhao[2], Yanjiang Liu[1], Chenyue Qiu[6], Jehad Abed[1], Hengzhou Liu[7], Heejong Shin[7], Dingsheng Wang[5], Yadong Li[5], David Sinton[2] & Edward H. Sargent[1]

The electrochemical reduction of CO_2 in acidic conditions enables high single-pass carbon efficiency. However, the competing hydrogen evolution reaction reduces selectivity in the electrochemical reduction of CO_2, a reaction in which the formation of CO, and its ensuing coupling, are each essential to achieving multicarbon (C_{2+}) product formation. These two reactions rely on distinct catalyst properties that are difficult to achieve in a single catalyst. Here we report decoupling the CO_2-to-C_{2+} reaction into two steps, CO_2-to-CO and CO-to-C_{2+}, by deploying two distinct catalyst layers operating in tandem to achieve the desired transformation. The first catalyst, atomically dispersed cobalt phthalocyanine, reduces CO_2 to CO with high selectivity. This process increases local CO availability to enhance the C–C coupling step implemented on the second catalyst layer, which is a Cu nanocatalyst with a Cu–ionomer interface. The optimized tandem electrodes achieve 61% C_2H_4 Faradaic efficiency and 82% C_{2+} Faradaic efficiency at 800 mA cm^{-2} at 25 °C. When optimized for single-pass utilization, the system reaches a single-pass carbon efficiency of 90 ± 3%, simultaneous with 55 ± 3% C_2H_4 Faradaic efficiency and a total C_{2+} Faradaic efficiency of 76 ± 2%, at 800 mA cm^{-2} with a CO_2 flow rate of 2 ml min^{-1}.

Alkaline and neutral electrolytes are used to suppress the hydrogen evolution reaction (HER) and facilitate C–C coupling in the electrochemical CO_2 reduction reaction (CO_2RR)[1–7]. Unfortunately, in this case, over 75% of the input CO_2 is lost chemically by reacting with hydroxyl ions (OH^-) to form (bi)carbonates, the result of high local alkalinity at the cathode[8–12]. This lowers the single-pass conversion efficiency (SPCE) of CO_2 and imposes an energetic penalty to recover the lost CO_2 reactants[13–16].

Using acidic electrolytes for the CO_2RR can improve CO_2 utilization by reducing (bi)carbonate formation and CO_2 crossover[17–20]; however, the kinetically more facile HER typically outcompetes the CO_2RR in acidic media, leading to poor CO_2RR selectivity[21–23].

[1]Department of Electrical and Computer Engineering, University of Toronto, Toronto, Ontario, Canada. [2]Department of Mechanical and Industrial Engineering, University of Toronto, Toronto, Ontario, Canada. [3]Beijing Synchrotron Radiation Facility, Institute of High Energy Physics, Chinese Academy of Sciences, Beijing, China. [4]KU-KIST Graduate School of Converging Science and Technology, Korea University, Seoul, Republic of Korea. [5]Department of Chemistry, Tsinghua University, Beijing, China. [6]Department of Materials Science and Engineering, University of Toronto, Toronto, Ontario, Canada. [7]Department of Chemistry, Northwestern University, Evanston, IL, USA. [8]These authors contributed equally: Yuanjun Chen, Xiao-Yan Li, Zhu Chen. e-mail: ted.sargent@utoronto.ca

https://doi.org/10.1038/s41565-023-01543-8

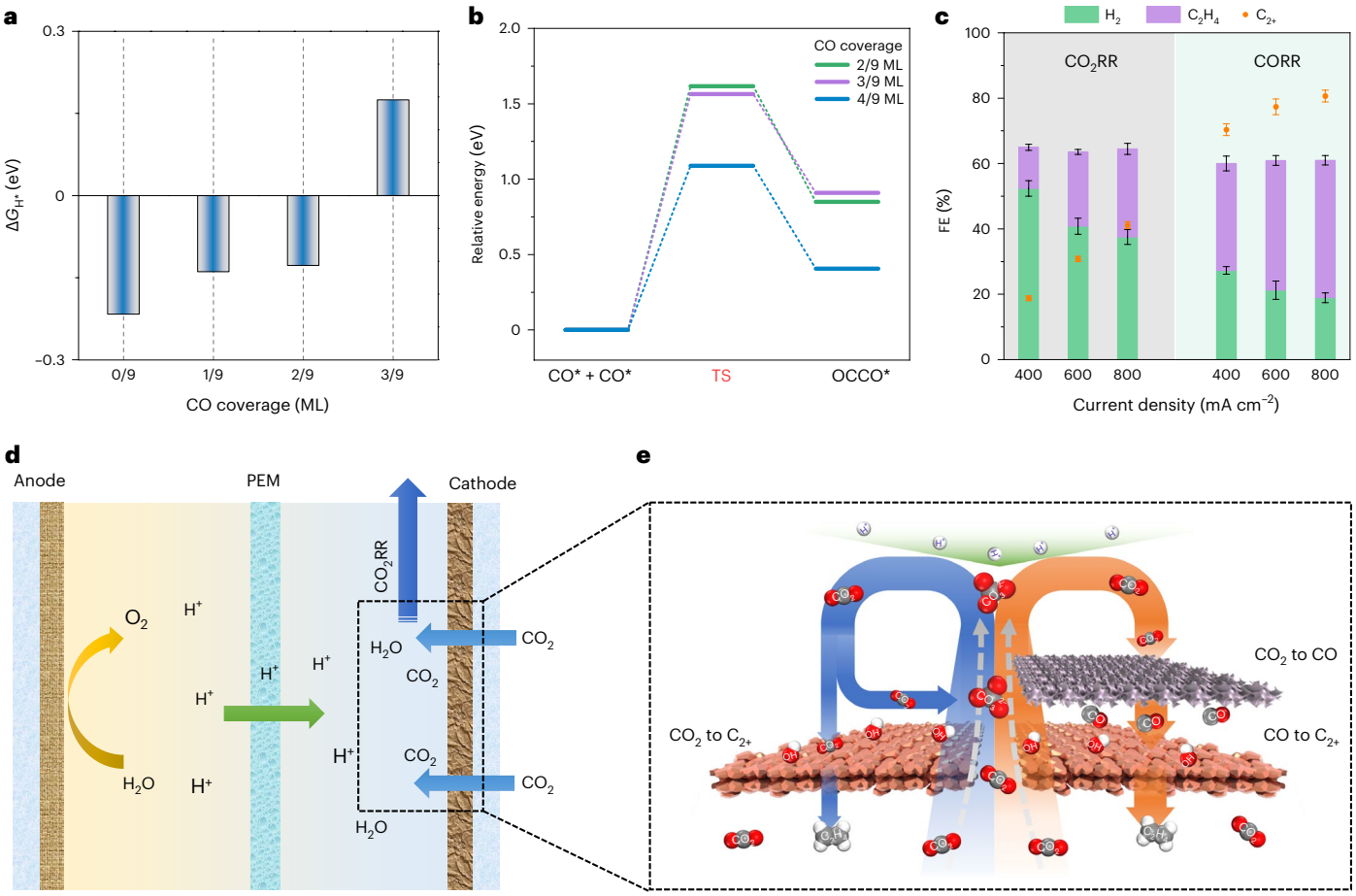

Fig. 1 | The spatially decoupled strategy for acidic CO_2RR via tandem catalysis. a, Reaction free energies for H* intermediate formation on the Cu surface under different CO coverages. ML, monolayer. **b**, Energy profiles for initial states, transition states (TSs) and final states of CO dimerization on the Cu surface under different CO coverages. **c**, FE values of H_2, C_2H_4 and C_{2+} on the Cu electrode in the CO_2RR and CORR at different current densities in an acidic buffer electrolyte of 0.5 M H_3PO_4 and 0.5 M KH_2PO_4 with 2.5 M KCl. Values are means, and error bars represent the standard deviation from three independent measurements ($n = 3$). **d**, Schematic of the ion transport and reactions in the acidic CO_2RR system. PEM, proton exchange membrane. **e**, Schematic illustration of the spatially decoupled strategy via tandem catalysis in the acidic CO_2RR system, showing CO_2 transport in the acidic CO_2RR system.

We pursued strategies that would promote selective C_{2+} formation in acidic conditions. It is held that high CO coverage assists in C–C coupling; however, we first checked that the forward rate of C–C coupling could indeed be promoted by a high presence of CO. Using density functional theory (DFT) we studied the reaction energetics of the CO_2RR on Cu, noting the dependence on the surface concentration of the reaction intermediates (that is, CO) and the adsorbed H (H*; * indicates a surface site)[22,24–26]. We found that greater CO coverage on Cu reduces the Gibbs free energy of H adsorption (ΔG_{H^*}), thus leading to a predicted increase in the HER overpotential[27–29] (Fig. 1a and Supplementary Figs. 1–3). We also saw that a lower energy barrier for the C–C coupling reaction appears at greater CO coverage on Cu (Fig. 1b). Experimentally, we switched the input gas from CO_2 to CO and found increased C_2H_4 and C_{2+} production and decreased H_2 Faradaic efficiency (FE; Fig. 1c). These computational and experimental results motivated us to seek routes to generate a high local concentration of CO on the catalyst surface.

Noting that to achieve each goal—first CO generation and then C–C coupling—relies on very distinct catalyst properties[30–35], we pursued a spatially decoupled strategy, that is, a tandem approach (Fig. 1d,e). We employed one catalyst optimized for the first chemical transformation of CO_2 to CO, and a distinct (but proximate, at the nanoscale) second catalyst for CO to C_{2+}.

To implement the first step—CO_2 to CO in acidic media—we began with a known high-rate high-selectivity catalyst: carbon-supported cobalt phthalocyanine (CoPc/C; synthesis details in the Methods). This catalyst has shown excellent CO selectivity in alkaline conditions[4]. Unfortunately, we found in early experimental studies that simply transferring this CoPc/C catalyst did not result in high selectivity in acidic conditions (Supplementary Figs. 4 and 5). Its FE was limited to 70% CO. This performance declined rapidly over the course of 2 hours. Using high-resolution transmission electron microscopy (TEM), we observed Co agglomeration, indicating the primary cause of this selectivity loss: the agglomeration of CoPc, triggered by the desorption of CoPc from the support surface (Supplementary Fig. 6).

We posited that a uniform dispersion of CoPc molecules on a strongly interacting support could enable a higher initial FE to be achieved and maintained over the course of catalyst operation. This motivated us to pursue CoPc atomically dispersed on a hollow carbon (HC) support (CoPc@HC), where the individual CoPc molecules are anchored to the support. The support we obtained through the pyrolysis of a core–shell composition (ZIF-8@PZS) of poly(cyclotriphospazene-co-4,4′-sulfonyldiphenol) (PZS) coated onto a zeolitic imidazolate framework (ZIF-8; Supplementary Fig. 7 and Fig. 2a; details are in the Methods). The CoPc@HC catalyst has a hollow morphology and no evidence of CoPc agglomeration (Fig. 2b,c and Supplementary Fig. 8). High-resolution *Z*-contrast images substantiate the atomic dispersion of Co species, as indicated by the individual bright dots associated with the Co centres of CoPc molecules

https://doi.org/10.1038/s41565-023-01543-8

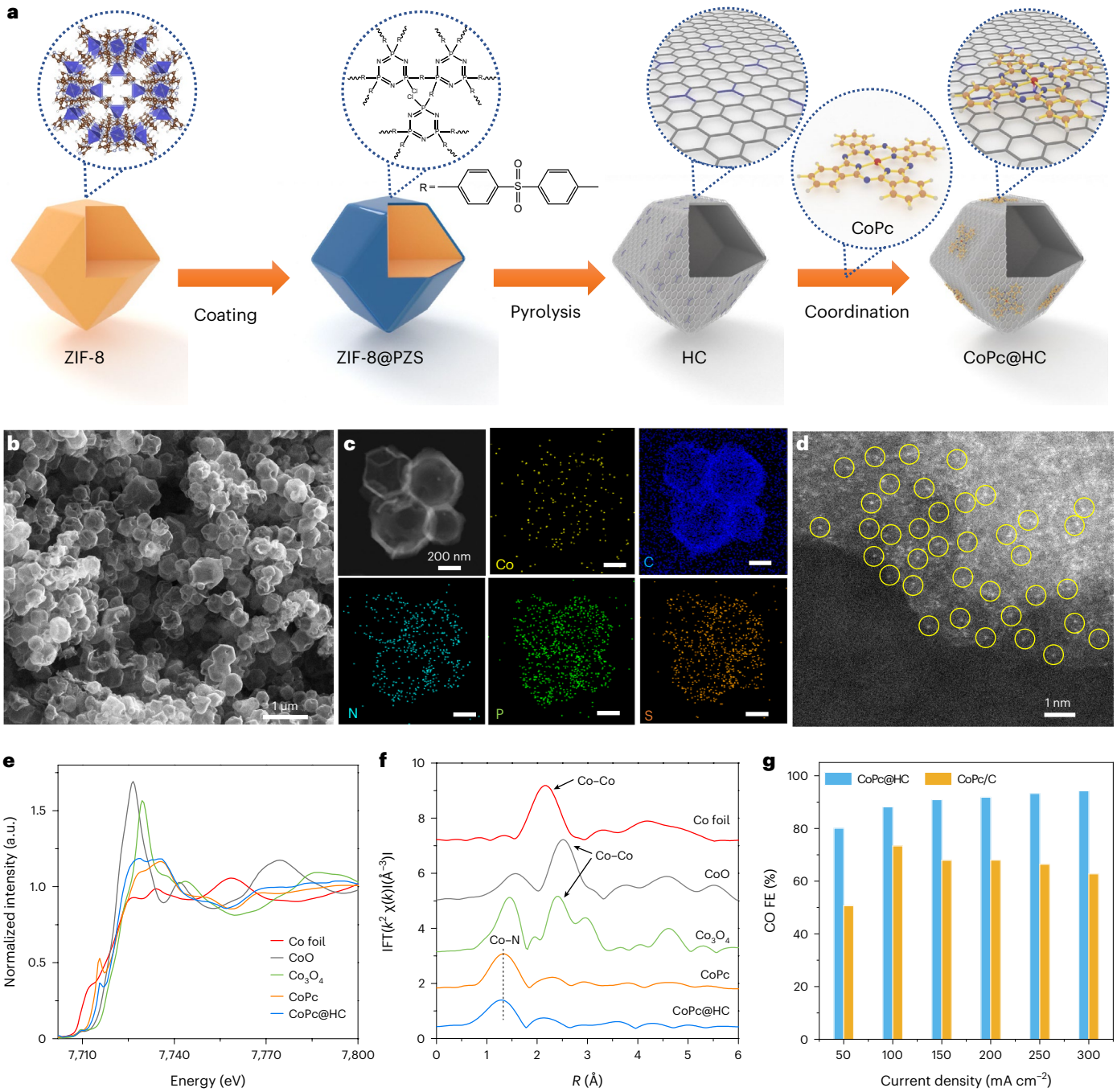

Fig. 2 | Synthesis and structural analysis of atomically dispersed CoPc@HC. **a**, Schematic illustration of the synthesis process of CoPc@HC. ZIF-8@PZS is a core–shell composition of PZS coated onto ZIF-8. **b**, SEM image of CoPc@HC. **c**, High-angle annular dark-field scanning TEM (HAADF-STEM) image and the corresponding energy dispersive spectroscopy mapping images (Co, yellow; C, blue; N, dark green; P, green; S, orange) of CoPc@HC. **d**, Aberration-corrected HAADF-STEM image of CoPc@HC. The individual bright dots marked by yellow circles are associated with the Co centres of CoPc molecules. **e**, Co K-edge X-ray absorption near-edge structure (XANES) spectra of CoPc@HC and reference samples (Co foil, CoO, Co_3O_4, CoPc). **f**, Magnitude of Fourier-transformed Co K-edge extended X-ray absorption fine structure spectroscopy (EXAFS) spectra of CoPc@HC and reference samples. $\chi(k)$ is the extracted EXAFS signal, k is the photoelectron momentum and R is the radial distance without phase correction. **g**, Comparison of CO FE on CoPc@HC electrode and CoPc/C electrode in acidic CO_2RR in an acidic buffer electrolyte of 0.5 M H_3PO_4 and 0.5 M KH_2PO_4 with 2.5 M KCl in a flow cell at 25 °C.

(Fig. 2d, Supplementary Note 1 and Supplementary Fig. 9). A strong catalyst–support interaction, to reduce Co agglomeration, is evidenced in X-ray absorption spectra that show a shift of the Co K edge of CoPc@HC to a higher-energy position, accompanied by an increase in the white-line peak intensity compared to the case of unsupported CoPc. These observations suggest an electronic interaction between CoPc and the N species on the HC support (Fig. 2e,f as well as Supplementary Note 2, Supplementary Figs. 10–16 and Supplementary Table 1). Brunauer–Emmett–Teller measurements show that CoPc@HC exhibits a Brunauer–Emmett–Teller surface of 1,087 $m^2 g^{-1}$ (Supplementary Fig. 17), something that we propose may facilitate mass transport of CO_2 gas and intermediates.

The CoPc@HC catalyst produced a CO FE of 94% and H_2 FE of <3% at 300 mA cm^{-2} (Fig. 2g). This was retained to within 3% relative to

the initial value over 12 h of operation at 300 mA cm^{-2} (Supplementary Figs. 18–20). Structural characterization of the used CoPc@HC catalyst after a 12 h stability test showed that the structure of CoPc was well-preserved (Supplementary Fig. 21). These performance metrics exceed those of previously reported CO_2-to-CO catalysts in acidic media (Supplementary Table 2).

We then turned our attention to the tandem catalyst, one that would unite on a single support the CO_2–CO and the C–C coupling steps. Reasoning that CO, with its low solubility in aqueous electrolyte, would not dissolve efficiently therein, we placed the CO-producing layer on top such that a CO concentration gradient, from the CO-producing layer to the C–C coupling catalyst layer, would be generated. This, we posited, could drive CO downwards, through the C–C coupling catalyst layer, to promote the desired reaction sequence and local enrichment.

With this in mind, we designed a tandem electrode consisting of the C–C coupling catalyst followed by an upper layer of CO_2-to-CO catalyst as described above. We first added the CoPc@HC catalyst on the top of the sputtered Cu (sCu) layer to construct a CoPc@HC/sCu tandem electrode. We evaluated its acidic CO_2RR performance using a flow cell electrolyser in a buffered acidic electrolyte containing 0.5 M H_3PO_4, 0.5 M KH_2PO_4 and 2.5 M KCl. The dominant product generated by the CoPc@HC/sCu tandem electrode was CO, and the FE to C_{2+} reached a maximum value of 36% at 200 mA cm^{-2}. A further increase in current density led to a decrease in C_{2+} formation while the CO FE remained nearly constant (Supplementary Fig. 22). We posited that the low C_{2+} FE is a result of underused CO generated by the CoPc@HC layer. We addressed this challenge by increasing the density of Cu sites and enhancing the mass transport of CO to these active sites. We introduced a three-dimensional Cu–ionomer interface catalyst layer consisting of Cu nanoparticles (NPs) coated by ionomer between the CoPc@HC and sputtered Cu to build up a CoPc@HC/Cu tandem electrode (Fig. 3a–c and Supplementary Figs. 23 and 24). In this tandem electrode configuration, CO_2 gas first goes through the gas diffusion layer and the ionomer-modified Cu NP layer, and finally reaches the CoPc@HC catalyst layer to be converted to CO. Once CO is formed, it diffuses back to the Cu NP layer and undergoes C–C coupling on the Cu surface to produce C_2H_4 and other C_{2+} products (Fig. 3d).

We then optimized the CoPc@HC/Cu tandem electrode by tuning the size of Cu NPs and the type of ionomers, and by varying the electrode configuration (Supplementary Note 3 and Supplementary Figs. 25–28). We also investigated the effect of electrolytes, including tuning the concentration of KCl, varying the anions and changing the type of acidic electrolyte (Supplementary Note 4 and Supplementary Figs. 29 and 30). By using the optimized CoPc@HC/Cu tandem electrode with 25 nm Cu NPs coated with perfluorosulfonic acid (PFSA) ionomer in a buffered acidic electrolyte containing 0.5 M H_3PO_4, 0.5 M KH_2PO_4 and 2.5 M KCl, we achieved an increase in the FE of C_2H_4 from 30% to 54%, and the C_{2+} increased from 36% to 80%; these were accompanied by a fourfold increase in the total current density to 800 mA cm^{-2} (Fig. 3e). An additional three independent experiments were performed to prepare the CoPc@HC/Cu tandem electrode and evaluate its performance. The acidic CO_2RR performance was consistently achieved, suggesting a good reproducibility (Supplementary Fig. 31).

The improvement in performance suggests that a greater local CO availability enabled by the tandem catalysis design promotes the formation of C_2H_4 and C_{2+} products. By contrast, a Cu electrode without a tandem configuration displayed much lower FE values for C_2H_4 (27%) and C_{2+} (41%; Fig. 3f,g). The CoPc@HC/Cu tandem electrode exhibited <10% H_2 FE compared with >35% in the case of the Cu electrode. We also assessed the stability in a flow cell electrolyser. The system maintained ~54% C_2H_4 FE for 16 h, and a scanning electrode microscopy (SEM) image showed that the bilayer structure remained intact (Supplementary Figs. 32–34).

The role of the first catalyst layer, CoPc@HC, is to generate a high CO flux to create a CO-rich environment for the second Cu catalyst layer. This high CO flux suppresses the competing HER and promotes C_{2+} production on the Cu surface in acidic media (Supplementary Note 5 and Supplementary Figs. 35 and 36). These results are consistent with DFT predictions wherein higher CO concentrations on the Cu surface lower the barrier to C–C coupling and suppress the HER. We attempted to mix CoPc@HC and Cu NPs into a one-layer tandem electrode. This one-layer tandem configuration leads to a substantial reduction in the interfacial CO concentration, which exhibited an increased HER and decreased FE values of C_2H_4 and C_{2+} in the acidic CO_2RR (Supplementary Fig. 37). We also observed that using a pure CO feed resulted in the highest C_2H_4 FE in a flow cell in acidic conditions (Supplementary Fig. 38). These results indicate that a higher CO flux is desired in an acidic CO_2RR environment, whereas Wang et al. reported an optimal C_2H_4 FE at a pH > 7 in an H-cell set-up under a CO_2/CO co-feeding environment or an internal CO_2/CO self-co-feeding environment using the mixed-one-layer tandem architecture of Cu/Ni–N-doped carbon[31].

While the CO_2RR is occurring, a fraction of the CO_2 dissolves into the electrolyte and reacts with local OH^- to become (bi)carbonate. When we model the reaction and diffusion species in an acidic CO_2RR, we observe an increase in the surface pH under higher operating current densities; this we assign to a local proton consumption rate that exceeds the rate of proton diffusion (Supplementary Note 6, Supplementary Figs. 39 and 40 and Supplementary Table 3). Despite an elevated pH (pH = ~9–13) at the catalyst surface, the electrolyte pH in the vicinity of the cathode decreases to its bulk value. This suggests that carbonate species formed locally will be converted back to CO_2 for subsequent reduction, preventing carbonate crossover. This part of CO_2 would be reduced into CO on the CoPc@HC catalyst layer and then react on the ionomer-modified Cu layer. Additionally, a higher CO_2 SPCE can benefit from the decoupled strategy since CO will not convert back to carbonate in a local alkaline environment (Fig. 1b). The experimental results are consistent with the idea that the two-layer tandem electrode configuration enables increased SPCE from 52% to 87% under consistent conditions (Fig. 3h, Supplementary Figs 41–43 and Supplementary Note 7).

The CoPc@HC/Cu tandem electrode demonstrated higher current densities of C_2H_4 and C_{2+} at the lower potentials compared to those of the Cu electrode (Fig. 3i and Supplementary Figs. 44 and 45). This translated to better energy efficiency at the device level, achieving a full-cell voltage of 3.8 V at 500 mA cm^{-2}, leading to a 16% C_2H_4 energy efficiency (Supplementary Figs. 46–51). This compares favourably to the 7% energy efficiency of the prior report[18]. Technoeconomic analysis shows the energy intensity of C_2H_4 production is 300 GJ $tonne^{-1}$, which is 50% lower compared to a high-efficiency prior CO_2-to-C_2H_4 conversion in an acidic system[18], and also compares well with benchmark alkaline and neutral systems that suffer substantial energy penalties associated with CO_2 separation[1,36] (Supplementary Notes 8 and 9, Supplementary Tables 4–6 and Supplementary Fig. 52).

We further noted that the C_2H_4 FE and C_{2+} FE for the CoPc@HC/Cu tandem electrode were higher than those values for the Cu electrode in the CO reduction reaction (CORR) where the availability of CO is not a limiting factor in C_2H_4 formation (Supplementary Figs. 53–56). We sought to examine further the interfacial structure between CoPc@HC and Cu nanoparticles. High-resolution TEM images and energy dispersive spectroscopy mapping as well as intensity profiles indicate a subnanometre spacing between CoPc@HC and Cu NPs (Supplementary Note 10 and Supplementary Figs. 57 and 58). We performed DFT to study the CO_2RR pathway on a periodic Cu slab covered by a CoN_4–C layer (Supplementary Fig. 59), which showed that the CoN_4–C/Cu model reduced the reaction energy required for C–C coupling by about 0.11 eV and changed the favourable reaction pathway for the hydrogenation of *CCO to favour C_2H_4 formation (Fig. 4a,b and Supplementary Figs. 60 and 61). We then tested the control sample without subnanometre-thick spaces between CoPc@HC and Cu particles and observed a decrease in C_2H_4 selectivity (Supplementary

https://doi.org/10.1038/s41565-023-01543-8

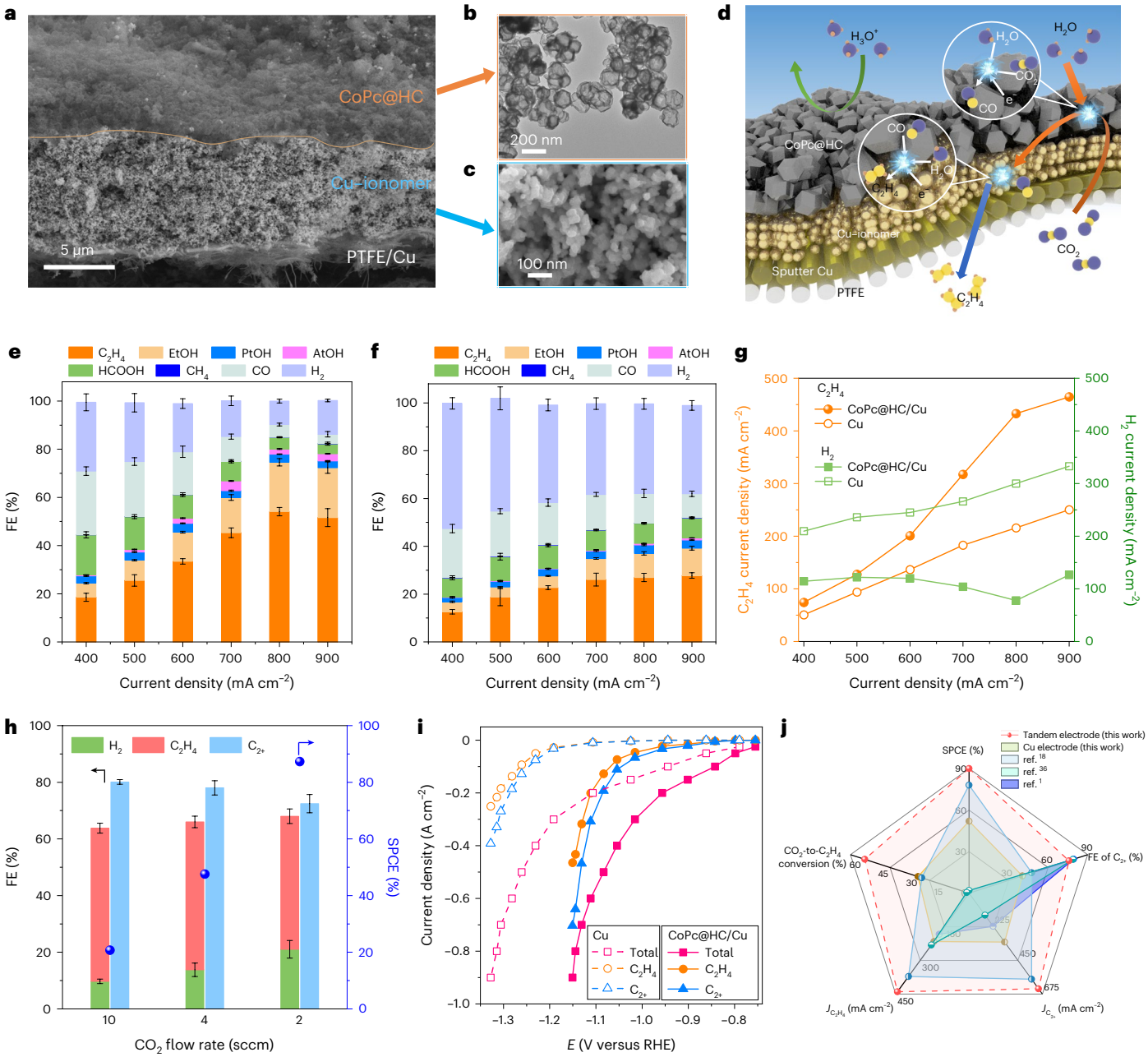

Fig. 3 | Acidic CO_2RR performance. a, Cross-sectional SEM image of CoPc@HC/Cu tandem electrode. PTFE, polytetrafluoroethylene. **b**,**c**, TEM image of upper CoPc@HC catalyst layer (**b**) and SEM image of lower Cu catalyst layer with the Cu–ionomer interface (**c**). **d**, Schematic of the spatially decoupled strategy via tandem catalysis, showing the electron (e^-) transfer and mass transport in acidic CO_2RR. **e**,**f**, FE values of CO_2RR products on the CoPc@HC/Cu tandem electrode (**e**) and Cu electrode (**f**) in an acidic buffer electrolyte of 0.5 M H_3PO_4 and 0.5 M KH_2PO_4 with 2.5 M KCl in a flow cell at 25 °C. The flow rate of the inlet CO_2 is 10 sccm. Values are means, and error bars represent the standard deviation from three independent measurements ($n = 3$). **g**, Partial current densities of C_2H_4 and H_2. **h**, FE values of CO_2RR products and SPCE on the CoPc@HC/Cu tandem electrode at 800 mA cm^{-2} with different inlet flow rates of CO_2 in an acidic buffer electrolyte of 0.5 M H_3PO_4 and 0.5 M KH_2PO_4 with 2.5 M KCl in a flow cell at 25 °C. Values are means, and error bars represent the standard deviation from three independent measurements ($n = 3$). **i**, Current density towards CO_2RR products on the CoPc@HC/Cu tandem electrode and Cu electrode in an acidic buffer electrolyte of 0.5 M H_3PO_4 and 0.5 M KH_2PO_4 with 2.5 M KCl in a flow cell at 25 °C. RHE, reversible hydrogen electrode. **j**, Comparison of the SPCE, FE and partial current density of C_{2+} ($J_{C_{2+}}$) partial current density of ethylene ($J_{C_2H_4}$) and CO_2-to-ethylene conversion of the CoPc@HC/(Cu + CoPc@HC) tandem electrode with those of state-of-the-art electrodes[1,18,36].

Fig. 62). The combined DFT and empirical results suggest that CoPc working in conjunction with Cu influences C_2H_4 selectivity in addition to promoting C–C coupling.

With the goal of applying this finding to a new electrode design for higher C_2H_4 production, we further increased the spacing between CoPc@HC and Cu particles by constructing a CoPc@HC/(Cu + CoPc@HC) tandem electrode (measured structure and composition in Supplementary Figs. 63 and 64 and Supplementary Note 11). This led to a 61% C_2H_4 FE and an 82% C_{2+} FE at 800 mA cm^{-2}. When optimized for single-pass carbon utilization with a 2 ml min^{-1} CO_2 flow rate, this led to a SPCE of 90 ± 3%, surpassing a prior report[18] (Fig. 3j and Supplementary Fig. 65); this high SPCE was achieved simultaneously with a C_2H_4 FE of 55 ± 3% and a C_{2+} FE of 76 ± 2% at 800 mA cm^{-2} (Supplementary Figs. 66–68 and Supplementary Note 12).

https://doi.org/10.1038/s41565-023-01543-8

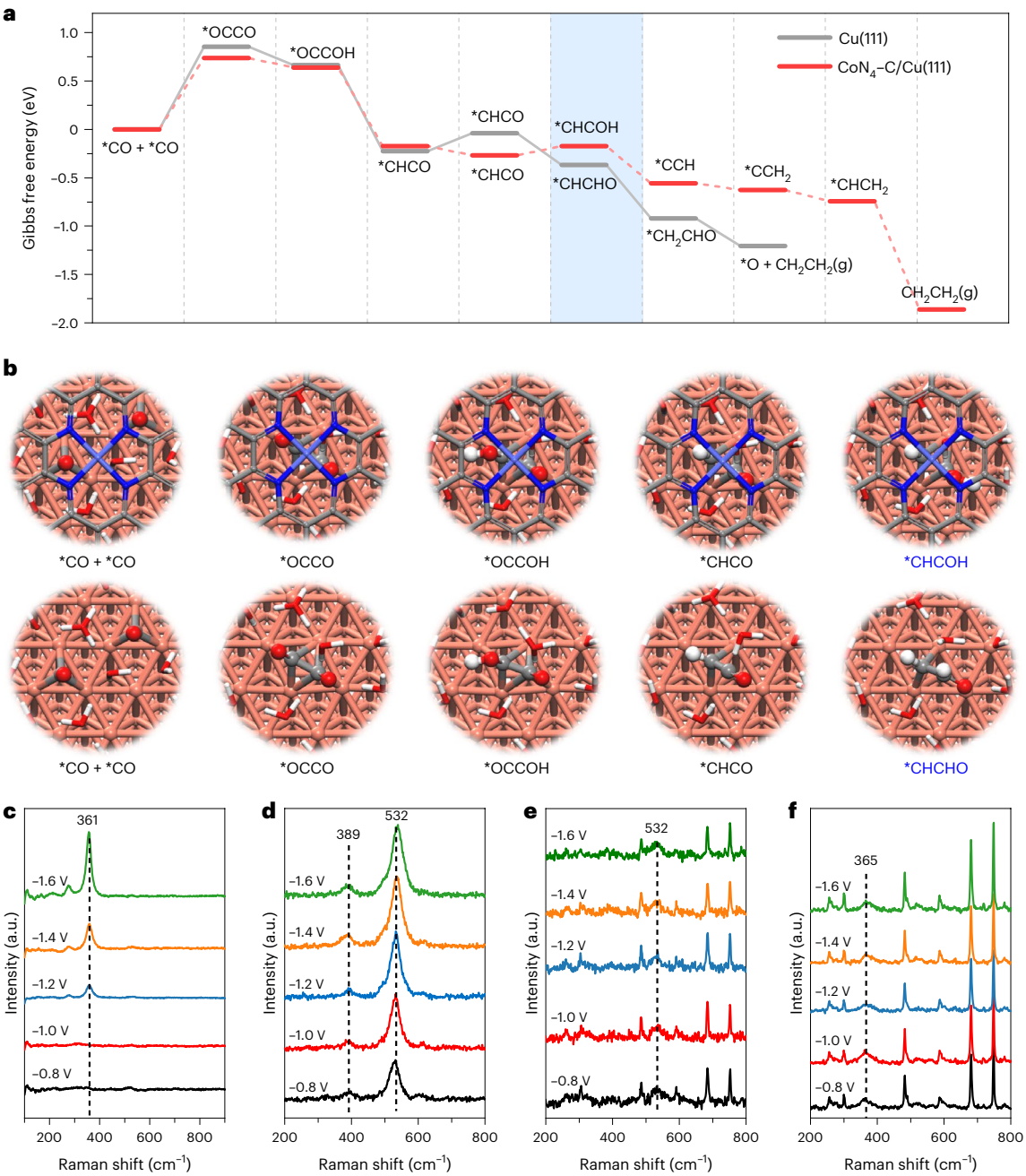

Fig. 4 | DFT calculations and in situ Raman measurements. a, Free energy diagram of CO_2RR on CoN_4–C/Cu tandem electrode and Cu electrode. The blue shading highlights the differences in the hydrogenation process of intermediate *CCO in reaction pathways for ethylene production on CoN4–C/Cu tandem electrode and Cu electrode. **b**, The corresponding atomic configurations of key intermediates from CO to ethylene. **c**,**d**, In situ Raman spectra of Cu electrode (**c**) and CoPc/Cu tandem electrode (**d**) under different applied potentials at 25 °C. **e**, In situ Raman spectra of CoPc/Cu tandem electrode with high CoPc coverage on the Cu surface at 25 °C. **f**, In situ Raman spectra of CoPc/Cu tandem electrode with agglomerated CoPc on the Cu surface at 25 °C.

Seeking to elucidate the interaction between CO and the tandem electrode, we probed CO adsorption on the Cu surface using in situ Raman spectroscopy. The peak at 361 cm^{-1} that emerged at −1.2 V versus Ag/AgCl in the Raman spectra of Cu is ascribed to the Cu–CO stretch, indicating that CO_2 is converted to CO on the Cu surface (Fig. 4c). In the Raman spectra of the CoPc/Cu tandem electrode (Fig. 4d), the peak at 361 cm^{-1} is blueshifted to 389 cm^{-1}, indicating a stronger binding of CO on the Cu sites as a result of CoPc in the vicinity of adsorbed CO. Additionally, we ascribe a new peak at 532 cm^{-1} to the Co–CO bending vibration effectuated by the interaction between CO and the Co species in CoPc molecules. A similar peak position has been observed for Fe–CO (refs. 37,38). We note that the Cu–CO and Co–CO peaks appear at −0.8 V for CoPc/Cu, indicating a much earlier onset compared to that observed on the bare Cu surface. This finding agrees with a picture wherein the presence of CoPc facilitates CO_2-to-CO conversion at lower overpotentials, which explains the lower CO_2RR voltage achieved using the tandem electrode herein than the Cu electrode. Control experiments indicate that higher CoPc coverage on the Cu surface is correlated primarily with a Co–CO peak at 532 cm^{-1} (Fig. 4e). Interestingly, when the CoPc forms aggregates, it is not effective at catalysing CO_2-to-CO conversion, and only the Cu–CO peak at 365 cm^{-1} is observed (Fig. 4f). The Raman results suggest that uniform coverage of CoPc molecules

on Cu is necessary to the tandem catalysis concept, a finding that motivates the implementation of atomically dispersed CoPc@HC.

Conclusions

In this work we studied the enrichment of CO coverage on the Cu surface to suppress the HER and promote multicarbon (C_{2+}) product formation in an acidic CO_2RR. This involved decoupling the overall CO_2-to-C_{2+} reaction into two steps—CO_2 to CO and CO to C_{2+}—each implemented in the integrated tandem catalyst. This led to a 61% C_2H_4 FE and 82% C_{2+} FE at 800 mA cm^{-2} while maintaining <10% H_2 FE. The system exhibited a C_2H_4 energy efficiency of 16%, a twofold improvement over an efficient prior report of acidic CO_2-to-C_2H_4 electrosynthesis.

The cascade CO_2–CO–C_{2+} combination of a solid oxide electrolyser cell and a CORR electrolyser provides an energy-efficient route for synthesizing C_{2+} products. However, the challenge lies in achieving stability and high SPCE. These systems are prone to carbon deposition, also known as coking[39], which affects stability at high conversion conditions (SPCE, >40%)[40]. The low conversion of the step involving the first solid oxide electrolyser cell requires a further separation step to separate the produced CO from unreacted CO_2 prior to the second electrolyser. The separation unit, the use of high-temperature materials and the second CORR electrolyser require significant capital investment and complex system configurations. The need for medium-grade to high-grade heat (>800 °C) imposes additional limitations on the operating scenarios of these systems. Therefore, a direct conversion of CO_2 to C_{2+} in a single carbonate-free acidic electrolyser offers a low-temperature alternative towards C_{2+} product synthesis[41]. Our tandem acidic CO_2RR system achieved a SPCE of 90% simultaneously with a C_2H_4 FE of 55% and a total C_{2+} FE of 76% at 800 mA cm^{-2}. Technoeconomic analysis showcased that this tandem system delivered a low energy cost for C_2H_4 production compared to state-of-the-art alkaline/neutral/acidic systems.

In neutral and alkaline systems, the presence of a high concentration of cations results in severe salt precipitation. In acidic electrolyte, the high concentration of protons within the diffusion layer and the lower local pH decreases the effects of salt precipitation. To tackle the challenges of salt precipitation and achieve industrial-level stability in future research on an acidic CO_2RR, more effort can be made in employing pure acids as electrolytes and devising strategies to replace alkali cations. This can involve the design of immobilized cation groups directly onto the catalyst or their incorporation within the membrane or electrolyte.

Online content

Any methods, additional references, Nature Portfolio reporting summaries, source data, extended data, supplementary information, acknowledgements, peer review information; details of author contributions and competing interests; and statements of data and code availability are available at https://doi.org/10.1038/s41565-023-01543-8.

References

1. Dinh, C. T. et al. CO_2 electroreduction to ethylene via hydroxide-mediated copper catalysis at an abrupt interface. *Science* **360**, 783–787 (2018).
2. Birdja, Y. Y. et al. Advances and challenges in understanding the electrocatalytic conversion of carbon dioxide to fuels. *Nat. Energy* **4**, 732–745 (2019).
3. Gao, D., Arán-Ais, R. M., Jeon, H. S. & Roldan Cuenya, B. Rational catalyst and electrolyte design for CO_2 electroreduction towards multicarbon products. *Nat. Catal.* **2**, 198–210 (2019).
4. Ren, S. et al. Molecular electrocatalysts can mediate fast, selective CO_2 reduction in a flow cell. *Science* **365**, 367–369 (2019).
5. Wu, Y., Jiang, Z., Lu, X., Liang, Y. & Wang, H. Domino electroreduction of CO_2 to methanol on a molecular catalyst. *Nature* **575**, 639–642 (2019).
6. Choi, C. et al. Highly active and stable stepped Cu surface for enhanced electrochemical CO_2 reduction to C_2H_4. *Nat. Catal.* **3**, 804–812 (2020).
7. Chen, C. et al. Boosting the productivity of electrochemical CO_2 reduction to multi-carbon products by enhancing CO_2 diffusion through a porous organic cage. *Angew. Chem. Int. Ed.* **61**, e202202607 (2022).
8. Weng, L.-C., Bell, A. T. & Weber, A. Z. Towards membrane-electrode assembly systems for CO_2 reduction: a modeling study. *Energy Environ. Sci.* **12**, 1950–1968 (2019).
9. Jeng, E. & Jiao, F. Investigation of CO_2 single-pass conversion in a flow electrolyzer. *React. Chem. Eng.* **5**, 1768–1775 (2020).
10. Ma, M. et al. Insights into the carbon balance for CO_2 electroreduction on Cu using gas diffusion electrode reactor designs. *Energy Environ. Sci.* **13**, 977–985 (2020).
11. Ma, M., Kim, S., Chorkendorff, I. & Seger, B. Role of ion-selective membranes in the carbon balance for CO_2 electroreduction *via* gas diffusion electrode reactor designs. *Chem. Sci.* **11**, 8854–8861 (2020).
12. Cofell, E. R., Nwabara, U. O., Bhargava, S. S., Henckel, D. E. & Kenis, P. J. A. Investigation of electrolyte-dependent carbonate formation on gas diffusion electrodes for CO_2 electrolysis. *ACS Appl. Mater. Inter.* **13**, 15132–15142 (2021).
13. Iizuka, A. et al. Carbon dioxide recovery from carbonate solutions using bipolar membrane electrodialysis. *Sep. Purif. Technol.* **101**, 49–59 (2012).
14. Al-Mamoori, A., Krishnamurthy, A., Rownaghi, A. A. & Rezaei, F. Carbon capture and utilization update. *Energy Technol.* **5**, 834–849 (2017).
15. Keith, D. W., Holmes, G., St. Angelo, D. & Heidel, K. A process for capturing CO_2 from the atmosphere. *Joule* **2**, 1573–1594 (2018).
16. Sisler, J. et al. Ethylene electrosynthesis: a comparative techno-economic analysis of alkaline vs membrane electrode assembly vs CO_2–CO–C_2H_4 tandems. *ACS Energy Lett.* **6**, 997–1002 (2021).
17. Gu, J. et al. Modulating electric field distribution by alkali cations for CO_2 electroreduction in strongly acidic medium. *Nat. Catal.* **5**, 268–276 (2022).
18. Huang, J. E. et al. CO_2 electrolysis to multicarbon products in strong acid. *Science* **372**, 1074–1078 (2021).
19. Monteiro, M. C. O., Philips, M. F., Schouten, K. J. P. & Koper, M. T. M. Efficiency and selectivity of CO_2 reduction to CO on gold gas diffusion electrodes in acidic media. *Nat. Commun.* **12**, 4943 (2021).
20. Xie, Y. et al. High carbon utilization in CO_2 reduction to multi-carbon products in acidic media. *Nat. Catal.* **5**, 564–570 (2022).
21. Ooka, H., Figueiredo, M. C. & Koper, M. T. M. Competition between hydrogen evolution and carbon dioxide reduction on copper electrodes in mildly acidic media. *Langmuir* **33**, 9307–9313 (2017).
22. Bondue, C. J., Graf, M., Goyal, A. & Koper, M. T. M. Suppression of hydrogen evolution in acidic electrolytes by electrochemical CO_2 reduction. *J. Am. Chem. Soc.* **143**, 279–285 (2021).
23. Mariano, R. G. et al. Microstructural origin of locally enhanced CO_2 electroreduction activity on gold. *Nat. Mater.* **20**, 1000–1006 (2021).
24. Monteiro, M. C. O. et al. Absence of CO_2 electroreduction on copper, gold and silver electrodes without metal cations in solution. *Nat. Catal.* **4**, 654–662 (2021).
25. Banerjee, S., Gerke, C. S. & Thoi, V. S. Guiding CO_2RR selectivity by compositional tuning in the electrochemical double layer. *Acc. Chem. Res.* **55**, 504–515 (2022).
26. Nitopi, S. et al. Progress and perspectives of electrochemical CO_2 reduction on copper in aqueous electrolyte. *Chem. Rev.* **119**, 7610–7672 (2019).

27. Shi, C., Hansen, H. A., Lausche, A. C. & Norskov, J. K. Trends in electrochemical CO_2 reduction activity for open and close-packed metal surfaces. *Phys. Chem. Chem. Phys.* **16**, 4720–4727 (2014).
28. Zhong, M. et al. Accelerated discovery of CO_2 electrocatalysts using active machine learning. *Nature* **581**, 178–183 (2020).
29. Zhang, Y.-J., Sethuraman, V., Michalsky, R. & Peterson, A. A. Competition between CO_2 reduction and H_2 evolution on transition-metal electrocatalysts. *ACS Catal.* **4**, 3742–3748 (2014).
30. Liu, X. et al. Understanding trends in electrochemical carbon dioxide reduction rates. *Nat. Commun.* **8**, 15438 (2017).
31. Wang, X. et al. Mechanistic reaction pathways of enhanced ethylene yields during electroreduction of CO_2–CO co-feeds on Cu and Cu-tandem electrocatalysts. *Nat. Nanotechnol.* **14**, 1063–1070 (2019).
32. Chen, C. et al. Cu-Ag tandem catalysts for high-rate CO_2 electrolysis toward multicarbons. *Joule* **4**, 1688–1699 (2020).
33. Wang, H. et al. Synergistic enhancement of electrocatalytic CO_2 reduction to C_2 oxygenates at nitrogen-doped nanodiamonds/Cu interface. *Nat. Nanotechnol.* **15**, 131–137 (2020).
34. Wang, Y., Zheng, X. & Wang, D. Design concept for electrocatalysts. *Nano Res.* **15**, 1730–1752 (2022).
35. Seh, Z. W. et al. Combining theory and experiment in electrocatalysis: insights into materials design. *Science* **355**, eaad4998 (2017).
36. Li, F. et al. Molecular tuning of CO_2-to-ethylene conversion. *Nature* **577**, 509–513 (2020).
37. Li, F. et al. Cooperative CO_2-to-ethanol conversion via enriched intermediates at molecule–metal catalyst interfaces. *Nat. Catal.* **3**, 75–82 (2019).
38. Hung, S. F. et al. A metal-supported single-atom catalytic site enables carbon dioxide hydrogenation. *Nat. Commun.* **13**, 819 (2022).
39. Skafte, T. L. et al. Selective high-temperature CO_2 electrolysis enabled by oxidized carbon intermediates. *Nat. Energy* **4**, 846–855 (2019).
40. Yan, J. et al. High-efficiency intermediate temperature solid oxide electrolyzer cells for the conversion of carbon dioxide to fuels. *J. Power Sources* **252**, 79–84 (2014).
41. Ozden, A. et al. Carbon-efficient carbon dioxide electrolysers. *Nat. Sustain.* **5**, 563–573 (2022).

Publisher's note Springer Nature remains neutral with regard to jurisdictional claims in published maps and institutional affiliations.

Springer Nature or its licensor (e.g. a society or other partner) holds exclusive rights to this article under a publishing agreement with the author(s) or other rightsholder(s); author self-archiving of the accepted manuscript version of this article is solely governed by the terms of such publishing agreement and applicable law.

© The Author(s), under exclusive licence to Springer Nature Limited 2023

Methods

Chemicals

Cobalt phthalocyanine (CoPc), zinc nitrate hexahydrate (98%), 2-methylimidazole (98%), cobaltous nitrate hexahydrate (98.5%), methanol, *N*,*N*-dimethylformamide (DMF), *N*,*N*-diethylethanamine, Nafion perfluorinated resin solution (5 wt% in a mixture of lower aliphatic alcohols and water; Sigma-Aldrich), phosphoric acid (85%), potassium chloride, potassium phosphate monobasic, sulfuric acid, potassium bromide and potassium sulfate were purchased from Sigma-Aldrich. Phosphonitrilic chloride trimer (98%) and bis(4-hydroxyphenyl) sulfone were purchased from Alfa Aesar. Alkaline ionomers XA-9 and XC-2 were purchased from Dioxide Materials. Copper nanoparticles (25 nm, 100 nm and 580 nm) were purchased from US Research Nanomaterials. The Nafion 117 membrane, platinum mesh and gas diffusion layer (Freudenberg H23C3) and carbon powder (Vulcan XC-72R) were received from Fuel Cell Store. The PTFE gas diffusion layer with 450 nm pore size was obtained from Beijing Zhongxingweiye Instrument Co. The copper target (>99.99%) was purchased from Kurt J. Lesker. The conductive gas diffusion layer was prepared by sputtering a 150 nm copper layer on the PTFE substrate using a pure copper target with a deposition rate of 1 Å s^{-1} in an Angstrom Nexdep sputtering system. Distilled water with a resistivity of 18.2 MΩ cm, obtained from a Milli-Q reference water purification system, was used to prepare the aqueous solutions in all the experiments. All chemicals were used without any further purification.

Synthesis of ZIF-8

Some 6 mmol $Zn(NO_3)_2{\cdot}6H_2O$, 24 mmol 2-methylimidazole and 100 ml methanol were mixed with vigorous stirring for 3 min at 25 °C. Subsequently, the mixture was kept at 35 °C for 6 h. The precipitate was collected, washed and finally dried in a vacuum at 80 °C for 12 h.

Synthesis of ZIF-8@PZS

Some 400 mg of as-prepared ZIF-8 powder was dispersed in 40 ml methanol. Then, 100 ml methanol containing 325 mg bis(4-hydroxyphenyl) sulfone and 152 mg phosphonitrilic chloride trimer was added and stirred for 15 min. Subsequently, 1 ml *N*,*N*-diethylethanamine was slowly dripped into the above dispersion, followed by stirring for 15 h at 25 °C. The resulting precipitate marked as ZIF-8@PZS was collected, washed and finally dried in a vacuum at 80 °C for 12 h.

Synthesis of HC

The as-prepared ZIF-8@PZS powder was placed in a quartz boat and maintained at 950 °C for 3 h in a tube furnace with a heating rate of 5 °C min^{-1} under a flowing Ar atmosphere to obtain HC.

Synthesis of CoPc@HC

Some 4 mg CoPc and 60 mg HC were dispersed separately in 60 ml DMF using sonication. Then, the CoPc dispersion solution was added to the HC suspension. The mixture was sonicated for 30 min and then stirred for 24 h at 25 °C. Subsequently, the CoPc@HC was obtained by washing with DMF many times until colourless, followed by drying in a vacuum at 80 °C for 12 h.

Electrode preparation

The state-of-the-art CoPc/C electrode was prepared according to a previously reported method[4]. In a typical procedure, 82.9 mg Vulcan carbon powder (XC-72R), 89.6 mg CoPc and 374 µl Nafion perfluorinated resin solution were stirred and sonicated in 35 ml absolute ethanol. Then, 10 ml of the ink was sprayed onto the gas diffusion layer (Freudenberg H23C3). The Cu electrode was prepared through airbrushing the catalyst ink, consisting of 30 mg Cu NPs, 2 ml methanol and 22.5 µl Nafion perfluorinated resin solution, onto a conductive gas diffusion layer with a Cu NP loading of 1 mg cm^{-2}. For the preparation of the CoPc@HC/Cu electrode, the catalyst ink comprising 15 mg CoPc@HC, 2 ml methanol and 45 µl Nafion perfluorinated resin solution was sprayed onto the Cu electrode with a CoPc@HC loading of 0.5 mg cm^{-2} using airbrushing. The CoPc@HC/sCu electrode was prepared by spraying CoPc@HC catalyst ink onto the sputtered Cu layer. The CoPc@HC electrode was prepared by spraying CoPc@HC catalyst ink onto the gas diffusion layer (Freudenberg H23C3). For the preparation of the Cu + CoPc@HC electrode, catalyst ink consisting of 30 mg Cu NPs and 6 mg CoPc@HC, 2 ml methanol and 22.5 µl Nafion perfluorinated resin solution was sprayed onto a conductive gas diffusion layer with a catalyst loading of 1 mg cm^{-2}. For the preparation of the CoPc@HC/(Cu + CoPc@HC) electrode, catalyst ink comprising 15 mg CoPc@HC, 2 ml methanol and 45 µl Nafion perfluorinated resin solution was sprayed onto the Cu + CoPc@HC electrode with a CoPc@HC loading of 0.5 mg cm^{-2} using airbrushing.

Material characterization

SEM images were obtained in a Hitachi field emission SEM SU5000 microscope. The high-resolution TEM images and the corresponding elemental mappings were collected on a JEOL JEM-2100F with an electron acceleration energy of 200 kV. The HAADF-STEM images were collected on a high-resolution TEM instrument (JEM-ARM200F working at 300 kV) equipped with a probe spherical aberration corrector. X-ray powder diffractometer measurements were performed in a MiniFlex600 with Cu Kα radiation. The metal content of the catalysts was measured by inductively coupled plasma optical emission spectroscopy (iCAP6300). X-ray photoelectron spectroscopy measurements were performed in an ECSA device (PHI 5700) with an Al Kα X-ray energy source (1,486.6 eV) for excitation. X-ray absorption spectroscopy measurements were carried out at the 9BM beamline of the Advanced Photon Source (Argonne National Laboratory, Lemont, Illinois, US). The X-ray absorption spectroscopy data were processed using ATHENA and ARTEMIS software incorporated into a standard IFEFFIT package. Nitrogen adsorption isotherms were acquired at 77 K using a Micromeritics 3-FLEX surface characterization analyser. Before measurement, the samples were subjected to vacuum degassing at 100 °C for 16 hours. The specific surface area was assessed using the Brunauer–Emmett-Teller method, while the pore volume was calculated from the quantity of nitrogen adsorbed at the relative pressure $P/P_0 = 0.99$ (P is absolute pressure and P_0 is the saturation vapour pressure of the adsorbate). Pore size distribution was determined using non-local DFT. In situ Raman measurements were conducted in a Renishaw inVia Raman microscope equipped with a water immersion objective (×63) and a 785 nm laser in a modified flow cell.

Electrochemical measurements

All the electrochemical measurements were performed at 25 °C. Unless otherwise specified, all the CO_2RR and CORR measurements were carried out in an electrochemical flow cell set-up at 25 °C using an electrochemical station (Autolab PGSTAT302N) equipped with a current booster (Metrohm Autolab, 10 A). Ag/AgCl (3 M KCl) and a Pt mesh were employed as the reference electrode and counter electrode, respectively. The cation-exchange membrane (Nafion 117) was used as the membrane to separate the cathode and anode chambers. Unless explicitly stated otherwise, all the CO_2RR and CORR measurements were carried out in an electrochemical flow cell set-up using 0.5 M phosphate buffer solution (0.5 M H_3PO_4, 0.5 M KH_2PO_4) with 2.5 M KCl as the catholyte and using the buffer solution of 0.5 M H_3PO_4 and 0.5 M KH_2PO_4 as the anolyte. Full-cell measurement was carried out in a slim flow cell set-up at 25 °C using 0.05 M H_2SO_4 with 2.5 M KCl as the catholyte and 0.05 M H_2SO_4 as the anolyte. The slim flow cell set-up comprises an anolyte chamber, catholyte chamber and gas flow chamber. The design of all chambers, as depicted in Supplementary Fig. 46, reduced the distance between the cathode and anode, minimizing ohmic losses. The cell was assembled by inserting a Nafion membrane between the cathode and anode compartments and applying equal compression torque

to all four fasteners. Assembled, the Nafion membrane was approximately 5 mm away from both the cathode and anode. For the full-cell measurement, 0.05 M H_2SO_4 with 2.5 M KCl was used as the catholyte, and 0.05 M H_2SO_4 was used as the anolyte. Titanium-mesh-supported iridium oxide (IrO_x/Ti-mesh) was used as the anode electrode and was prepared by a previously reported dip coating and thermal decomposition method[42]. In all the electrochemical tests, the gas products were analysed using a gas chromatograph (PerkinElmer Clarus 600). The liquid products were measured by ^{1}H NMR spectroscopy (600 MHz Agilent DD2 NMR spectrometer) with dimethyl sulfoxide (DMSO) as the reference standard and deuterium oxide (D_2O) as the lock solvent. The SPCE of CO_2 was assessed in an electrochemical flow cell set-up by varying the CO_2 flow rate in an acidic buffer electrolyte of 0.5 M H_3PO_4 and 0.5 M KH_2PO_4 with 2.5 M KCl as the catholyte, and an acidic buffer electrolyte of 0.5 M H_3PO_4 and 0.5 M KH_2PO_4 as the anolyte, at 800 mA cm^{-2}. To optimize the SPCE, we employed a CO_2 flow rate of 2 ml min^{-1} in a flow cell set-up with an electrode area of 1 cm^2. Data collection for SPCE commenced after maintaining an applied current density of 800 mA cm^{-2} for 30 minutes, thus ensuring that the system reached a steady state where the conversion between surface carbonate species and CO_2 had become substantially constant in time. The SPCE of CO_2 at the conditions of 298.15 K and 101.3 kPa was determined using the following equation:

$$\mathrm{SPCE} = ((j \times 60\,\mathrm{s})/(N \times F)) \div \left(\mathrm{flow\ rate}\,(1\,\mathrm{min}^{-1}) \times (1\ \mathrm{min})\right) / \left(24.05\,(1\,\mathrm{min}^{-1})\right)$$

where j is the partial current density of a specific group of products from CO_2 reduction and N is the electron transfer for every product molecule. F is the Faradaic constant.

The full-cell energy efficiency based on the production of ethylene was calculated as follows:

$$\mathrm{EE}_{\text{full cell, ethylene}} = \frac{(1.23 + (-E^0_{\text{ethylene}})) \times \mathrm{FE}_{\text{ethylene}}}{-E_{\text{full cell}}}$$

where E^0_{ethylene} is the thermodynamic potential of the conversion of CO_2 to ethylene ($E^0_{\text{ethylene}} = 0.08$ V versus RHE), $\mathrm{FE}_{\text{ethylene}}$ is the measured FE of ethylene and $E_{\text{full cell}}$ is the full-cell voltage without ohmic loss correction evaluated in the slim flow cell.

DFT calculations

The Vienna Ab initio Software Package was used to perform all DFT calculations, with the spin polarization setting[43,44]. The core–valence interaction was calculated by the projector augmented-wave method[45,46], where the Cu($d^{10}p^1$), Co(d^8s^1), O(s^2p^4), C(s^2p^2) and N(s^2p^3) electrons were treated as valence states, and the remaining electrons were seen as a core state. The cut-off energy was set to 450 eV. The exchange–correlation correction effect was described by the generalized gradient approximation in the Perdew–Burke–Ernzerhof functional[47]. For the geometry optimization, the self-consistent iteration must reach 10^{-5} eV for the energy convergence and 0.01 eV Å^{-1} for the force convergence. The DFT-D3 method was used to account for dispersion correction for van der Waals forces[48].

The 3 × 3 Cu(111) model was built, consisting of four layers of Cu atoms, in which the bottom two-atom layers were fixed to mimic the bulk material and the other atoms were relaxed. A charged water layer consisting of one protonated water molecule and five regular water molecules was considered to cover the Cu(111) surface. The vacuum space was about 15 Å along the z axis. The k-point mesh was set to 3 × 3 × 1 (ref. 49). The effect of a CO coverage of 0, 1/9 ML, 2/9 ML and 3/9 ML was measured to calculate the adsorption energy of H* and the reaction energy barrier of C–C coupling. The climbing-image nudged elastic band method was used to search the reaction transition states until the criteria of the force convergence and energy convergence reached 0.05 eV Å^{-1} and 10^{-5} eV (ref. 50), respectively.

The 6 × 6 Cu(111) model covered a charged water layer consisting of twenty-four water molecules, and a two-dimensional CoN_4–graphene monolayer structure was built. The bottom Cu layer was treated as the bulk material, and two atomic layers at the top were modelled as surfaces. The vacuum space was about 15 Å along the z axis. The k-point mesh was set to 2 × 2 × 1 (ref. 49). The different possible reaction pathways from CO to ethylene with/without the two-dimensional CoN_4–C structure were researched[51]. The optimum reaction pathways were studied to unravel the effect of the two-dimensional CoN_4–C structure.

Data availability

The authors declare that all data supporting the findings of this study are available within the paper and Supplementary Information files. Source data are provided with this paper.

References

42. Luc, W., Rosen, J. & Jiao, F. An Ir-based anode for a practical CO_2 electrolyzer. *Catal. Today* **288**, 79–84 (2017).
43. Kresse, G. & Hafner, J. *Ab initio* molecular dynamics for liquid metals. *Phys. Rev. B* **47**, 558–561 (1993).
44. Kresse, G. & Hafner, J. *Ab initio* molecular-dynamics simulation of the liquid-metal–amorphous-semiconductor transition in germanium. *Phys. Rev. B* **49**, 14251–14269 (1994).
45. Blochl, P. E. Projector augmented-wave method. *Phys. Rev. B* **50**, 17953–17979 (1994).
46. Kresse, G. & Joubert, D. From ultrasoft pseudopotentials to the projector augmented-wave method. *Phys. Rev. B* **59**, 1758–1775 (1999).
47. Perdew, J. P., Burke, K. & Ernzerhof, M. Generalized gradient approximation made simple. *Phys. Rev. Lett.* **77**, 3865–3868 (1996).
48. Grimme, S., Ehrlich, S. & Goerigk, L. Effect of the damping function in dispersion corrected density functional theory. *J. Comput. Chem.* **32**, 1456–1465 (2011).
49. Monkhorst, H. J. & Pack, J. D. Special points for Brillouin-zone integrations. *Phys. Rev. B* **13**, 5188–5192 (1976).
50. Henkelman, G., Uberuaga, B. P. & Jónsson, H. A climbing image nudged elastic band method for finding saddle points and minimum energy paths. *J. Chem. Phys.* **113**, 9901–9904 (2000).
51. Fan, Q. et al. Electrochemical CO_2 reduction to C_{2+} species: heterogeneous electrocatalysts, reaction pathways, and optimization strategies. *Mater. Today Energy* **10**, 280–301 (2018).

Acknowledgements

This work was financially supported by the Ontario Research Foundation's Research Excellence programme, the Natural Sciences and Engineering Research Council (NSERC) of Canada and TotalEnergies SE. This research used synchrotron resources of the Advanced Photon Source, an Office of Science User Facility operated for the US Department of Energy, Office of Science by Argonne National Laboratory, and was supported by the US Department of Energy under contract no. DE-AC02-06CH11357 as well as by the Canadian Light Source and its funding partners. All DFT computations were performed on the IBM BlueGene/Q supercomputer with support from the Southern Ontario Smart Computing Innovation Platform (SOSCIP) and the Niagara supercomputer at the SciNet HPC Consortium. SOSCIP is funded by the Federal Economic Development Agency of Southern Ontario, the Province of Ontario, IBM Canada Ltd, Ontario Centres of Excellence, Mitacs and 15 Ontario academic member institutions. SciNet is funded by the Canada Foundation for Innovation, the Government of Ontario, the Ontario Research Fund—Research Excellence and the University of Toronto. We acknowledge

the Ontario Centre for the Characterization of Advanced Materials (OCCAM) for characterization facilities. J.D. acknowledges financial support from the Youth Innovation Promotion Association of the Chinese Academy of Sciences (Y2022006).

Author contributions

E.H.S. supervised the project. Y.C. and E.H.S. conceived the idea. Y.C. designed the synthesis of the catalysts and carried out all the electrochemical experiments. X.-Y.L. with the help of P.O. carried out the DFT calculation. Z.C. performed the in situ Raman measurements. A.O. contributed to the preparation of IrO_x-coated Ti mesh electrodes and the energy assessment. J.D. and J.A. performed the X-ray absorption spectroscopy measurements. J.D. helped to analyse the X-ray absorption spectroscopy data. J.Z., Q.Q., X.W., S.W. and C.Q. helped to characterize the materials. S.L. performed the COMSOL simulation. J.E.H. contributed to manuscript editing. A.O., J.Z., B.-H.L., C.T., Y.X., R.K.M., Y.Z., Y. Liu, H.L., H.S. and D.S. assisted with the data analysis and discussions. D.W. and Y. Li contributed to the design of catalysts and assisted in conceiving the idea. Y.C., X.-Y.L., Z.C. and E.H.S. wrote the manuscript. All authors discussed the results and assisted during manuscript preparation.

Competing interests

There is a US provisional patent application (63/482.861) titled 'Electroreduction of CO_2 in acidic conditions using a catalyst having a dual CO generation and C-C coupling function' filed by the authors Y.C., X.-Y.L., Z.C. and E.H.S. and their institutions. The remaining authors declare no competing interests.

Additional information

Supplementary information The online version contains supplementary material available at https://doi.org/10.1038/s41565-023-01543-8.

Correspondence and requests for materials should be addressed to Edward H. Sargent.

Peer review information *Nature Nanotechnology* thanks Joel Ager III, Kazuhiro Takanabe and the other, anonymous, reviewer(s) for their contribution to the peer review of this work.

Reprints and permissions information is available at www.nature.com/reprints.